

# Synthesis-based Paradigm Free Mapping and analysis-based Total Activation perform identically for temporal deconvolution of fMRI data

Eneko Uruñuela<sup>a,b,\*</sup>, Thomas A.W. Bolton<sup>c</sup>, Younes Farouj<sup>d</sup>, Dimitri Van de Ville<sup>d,e</sup>, César Caballero-Gaudes<sup>a</sup>

<sup>a</sup>*Basque Center on Cognition, Brain and Language (BCBL), Donostia-San Sebastián, Spain.*

<sup>b</sup>*University of the Basque Country (EHU/UPV), Donostia-San Sebastián, Spain.*

<sup>c</sup>*Department of Decoded Neurofeedback, ATR Computational Neuroscience Laboratories, Kyoto, Japan*

<sup>d</sup>*Swiss Federal Institute of Technology Lausanne (EPFL), Lausanne, Switzerland.*

<sup>e</sup>*Faculty of Medicine of the University of Geneva, Geneva, Switzerland*

## Abstract

Functional MRI deconvolution algorithms are gaining popularity to study the dynamics of functional brain activity and connectivity at short timescales. This work sheds light on our understanding of two state-of-the-art approaches based on L1-norm regularized estimators: Paradigm Free Mapping (synthesis model) and Total Activation (analysis model). Through simulations with varying signal-to-noise ratios, and experimental data comprising a motor task and two resting-state datasets, we demonstrate that both techniques perform temporal deconvolution of fMRI data identically. In other words, the two methods yield identical estimates of the innovation and activity-inducing signals underlying BOLD events when an identical hemodynamic response function and regularization parameters are used. These observations open up the possibility for future developments without questioning their core formulation and performance.

**Keywords:** fMRI deconvolution, paradigm free mapping, total activation

## 1. Introduction

Functional magnetic resonance imaging (fMRI) data analyses are often directed to disentangling and understanding the neural processes that occur among brain regions. However, interactions in the brain are expressed, not at the level of hemodynamic responses, but at the neural level. Thus, an intermediate step that estimates the underlying neuronal activity is necessary for such analyses. Given the nature of the fMRI blood oxygenation level-dependent (BOLD) signal, the appropriate approximation of the neuronal activity can be obtained by means of deconvolution with an assumed hemodynamic response [1]. Simply put, deconvolution methods are capable of blindly estimating neuronal activity with no prior information on the timing of the BOLD events.

Deconvolution and methods alike are gaining popularity for exploring time-varying activity in fMRI data within a number of neuroimaging studies due to their potential to disentangle neural dynamics, especially when the information about the timing of the BOLD events is unknown, inaccurate, or insufficient. One of such cases is the study of resting-state fluctuations with the aim of gaining insight into the origin of the signals driving functional connectivity and its temporal dynamics, as well as the organizational principles of brain function; i.e. to

study and deconstruct the spatio-temporal structure of functional components that dynamically construct resting-state networks [2, 3, 4, 5, 6, 7, 8]. Another case in which the timing of the BOLD events is unknown is that of naturalistic paradigms, where subjects are shown a movie or story with the aim of detecting the functional structure of shared responses among a group of subjects and idiosyncratic patterns that could reveal meaningful individual differences [9, 10, 11, 12]. Furthermore, deconvolution techniques can prove to be helpful in clinical conditions to characterize functional alterations of patients with a progressive stage of multiple sclerosis at rest [13], to find functional signatures of prodromal psychotic symptoms and anxiety at rest on patients suffering from schizophrenia [14], to detect the foci of interictal events in epilepsy patients without an EEG recording [15], or to study functional dissociations observed during non-rapid eye movement sleep that are associated with reduced consolidation of information and impaired consciousness [16].

This note describes and compares synthesis- and analysis-based deconvolution methods for fMRI data and comprises three sections. In the first, we present the theory behind two state-of-the-art deconvolution approaches based on L1-norm regularized estimators: Paradigm Free Mapping (PFM) [17] — which is available as *3dPFM* and *3dMEPFM* in AFNI — and Total Activation (TA) [18]. We then assess their performance using the same hemodynamic response function with different criteria for the selection of the regularization parameter: a) a selection

\*Corresponding author

Email address: e.urunuela@bcbl.eu (Eneko Uruñuela)

55 based on the Bayesian (BIC) [19] and Akaike Information Criterion (AIC) [20], and b) a selection based on the estimated median absolute deviation (MAD) of the noise in the data. We report that both methods produce identical results when estimating the underlying activity-  
60 inducing and innovation signals in different signal-to-noise ratio (SNR) settings, and task-based and resting-state experimental datasets. In the final section, we discuss the pros and cons of each of the described techniques and conclude with our vision on potential extensions and developments for deconvolution algorithms for fMRI.  
65

## 2. Theory

The hemodynamic response to neuronal activity at time  $t$  can be modeled as the convolution with a finite impulse response function of the neuronal signal  $s_{t-\tau}$  at time  $t - \tau$  with the hemodynamic response function  $h_\tau$  [1]:

$$y_t = \sum_t h_\tau s_{t-\tau}, \quad (1)$$

where  $y_t$  is the measured BOLD signal on a given voxel. This equation can be reformulated in matrix notation as  $\mathbf{y} = \mathbf{H}\mathbf{s} + \epsilon$ , where  $\mathbf{y}, \mathbf{s} \in \mathbb{R}^N$ ,  $\mathbf{H} \in \mathbb{R}^{N \times N}$  is the HRF in Toeplitz matrix form,  $N$  is the number of frames of the fMRI acquisition, and  $\epsilon$  represents additional white Gaussian noise. The signal model in (1) can be extended to represent the neuronal signal  $\mathbf{s}$  in terms of its innovation signal  $\mathbf{u}$ , i.e. its derivative, and can be described as  $\mathbf{s} = \mathbf{L}\mathbf{u}$   
75 where  $\mathbf{L} \in \mathbb{R}^{N \times N}$  is an integration operator [21, 22].

Functional MRI data analyses are often directed to disentangling and understanding the neural processes that occur among brain regions. However, interactions in the brain are expressed, not at the level of hemodynamic responses, but at the neural level. Thus, an intermediate step that estimates the underlying neuronal activity is necessary for such analyses. Given the nature of the fMRI BOLD signal, the appropriate approximation of the neuronal activity can be obtained by means of deconvolution with an assumed hemodynamic response [1]. Hence, the maximum likelihood estimate of the hemodynamic response to the underlying neural activity can be calculated using the ordinary least-squares estimator that minimizes the residual sum of squares between the modeled ( $\mathbf{H}\mathbf{s}$ ) and measured ( $\mathbf{y}$ ) signals. Yet, the estimates of the neuronal activity  $\mathbf{s}$  must be constrained with a regularization term to attenuate the collinearity and high variability of the design matrix  $\mathbf{H}$ .  
80  
85  
90

### 2.1. Paradigm Free Mapping

Paradigm Free Mapping (PFM) builds upon the signal model introduced in (1); i.e., the BOLD signal is the result of convolving the underlying neural activity with the hemodynamic response, and proposes to estimate the

activity-inducing signal by solving the following regularized least-squares problem [17, 22, 23]:

$$\hat{\mathbf{s}} = \arg \min_{\mathbf{s}} \frac{1}{2} \|\mathbf{y} - \mathbf{H}\mathbf{s}\|_2^2 + \Omega(\mathbf{s}) \quad (2)$$

where  $\Omega(\mathbf{s})$  is the regularization term.

Assuming that single-trial BOLD responses are the result of brief bursts of neuronal activation, the activity-inducing signal  $\mathbf{s}$  must be a sparse vector. Thus, sparse estimates of  $\mathbf{s}$  could be obtained by substituting  $\Omega(\mathbf{s})$  in (3) with an  $l_0$ -norm and solving the optimization problem [24]. However, due to the convolution model defined in (3), finding the optimal solution to the problem demands an exhaustive search across all possible combinations of the columns of the design matrix  $\mathbf{H}$ . Hence, a pragmatic solution is to solve the optimization problem with the use of an  $l_1$ -norm, or LASSO [25], which is a convex function and therefore provides fast convergence to the optimal solution.

$$\hat{\mathbf{s}} = \arg \min_{\mathbf{s}} \frac{1}{2} \|\mathbf{y} - \mathbf{H}\mathbf{s}\|_2^2 + \lambda \|\mathbf{s}\|_1 \quad (3)$$

where  $\lambda$  regulates how sparse the optimal solution is.

Such formulation provides flexibility to expand the capabilities of PFM. For instance, incorporating the integration operator  $\mathbf{L}$  into the design matrix  $\mathbf{H}$  allows the recovery of the innovation signal  $\mathbf{u}$ ; i.e., the derivative of the activity-inducing signal  $\mathbf{s}$ . Therefore, the innovation signal can be estimated by solving the following optimization problem [21, 22]:

$$\hat{\mathbf{u}} = \arg \min_{\mathbf{u}} \frac{1}{2} \|\mathbf{y} - \mathbf{H}\mathbf{L}\mathbf{u}\|_2^2 + \lambda \|\mathbf{u}\|_1 \quad (4)$$

### 2.2. Total Activation

Even though based on the same signal model as PFM, Total Activation (TA) proposes to use a linear differential operator  $L_h$  that inverts the hemodynamic system based on activelets to recover the activity-inducing signal  $\mathbf{s}$  [18, 26, 27]:

$$L_h\{x\}(t) = s(t) \quad (5)$$

where  $x$  is the neuronal-related signal; i.e., the activity inducing signal  $\mathbf{s}$  convolved with the HRF, and  $L_h$  is defined as

$$L_h = \prod_{i=1}^{M_1} (D - \alpha_i I) \left( \prod_{j=1}^{M_2} (D - \gamma_j I) \right)^{-1} \quad (6)$$

where  $D$  is the derivative operator,  $\alpha_i (i = 1, \dots, M_1)$  define the zeros of the filter,  $\gamma_j (j = 1, \dots, M_2)$  represent the poles,  $I$  is the identity matrix and  $M_1 > M_2$ . Given the relationship between the activity-inducing and the innovation signal, the latter can be recovered as:

$$L\{x\}(t) = D\{s\}(t) = u(t) \quad (7)$$

where  $L = DL_h$  and  $D$  is the derivative.

Therefore, for a given voxel, the neuronal-related signal could be estimated by solving the following regularized least-squares problem:

$$\hat{\mathbf{x}} = \arg \min_{\mathbf{x}} \frac{1}{2} \|\mathbf{y} - \mathbf{x}\|_2^2 + \mathcal{R}(\mathbf{x}) \quad (8)$$

where  $\mathbf{y}$  is the fMRI data and  $\mathcal{R}(\mathbf{x})$  is the following  $l_1$ -norm regularization term:

$$\mathcal{R}(\mathbf{x}) = \lambda \sum_{t=1}^N \|\Delta_L \{\mathbf{x}\}\| \quad (9)$$

where  $\lambda$  is the regularization parameter.

This work evaluates the core of the two techniques, i.e. the regularized least-squares problem with temporal regularization, which corresponds to the generalized total-variation operator in Total Activation. Thus, we do not study the impact of spatial constraints, as we assume that spatial regularization terms should perform identically on both methods.

### 3. Results

A critical decision with deconvolution methods is the selection of the regularization parameter  $\lambda$ , for which many techniques have been proposed in the literature but an optimal is yet to be discovered. In fact, Paradigm Free Mapping and Total Activation base their selection of the regularization parameter on different criteria: the Bayesian Information Criterion (BIC) [19] and Akaike Information Criterion (AIC) [20], and a selection based on the convergence of the residuals to a pre-estimated level of the noise respectively. Hence, we compare the performance of the two algorithms with both selection criteria. Furthermore, we explore the differences between the techniques in terms of the estimation of the activity-inducing signal  $\mathbf{s}$  using the *spike model* in (3) and the innovation signal  $\mathbf{u}$  using the *block model* in (4).

#### 3.1. Simulated and experimental data

In order to compare the two methods while controlling for their correct performance, we simulated a 400 seconds ( $TR = 2$  s) activity-inducing signal with five neuronal events, convolved it with the SPMG1 HRF, and we added noise of different sources (physiological, thermal and motion-related) with different signal-to-noise ratios (SNR = [20 dB, 10 dB, 3 dB]) that represent low, medium and high levels of noise as shown in Figure 1.

Furthermore, we compared the two techniques on three datasets: a motor task and two resting-state acquisitions.

**Motor task dataset:** One healthy subject was scanned in a 3T MR scanner (Siemens) as part of a larger experiment under a Basque Center on Cognition, Brain and Language Review Board-approved protocol. T2\*-weighted multi-echo fMRI data was acquired with a multiband (MB) multi-echo gradient echo-planar imaging sequence (340 scans,

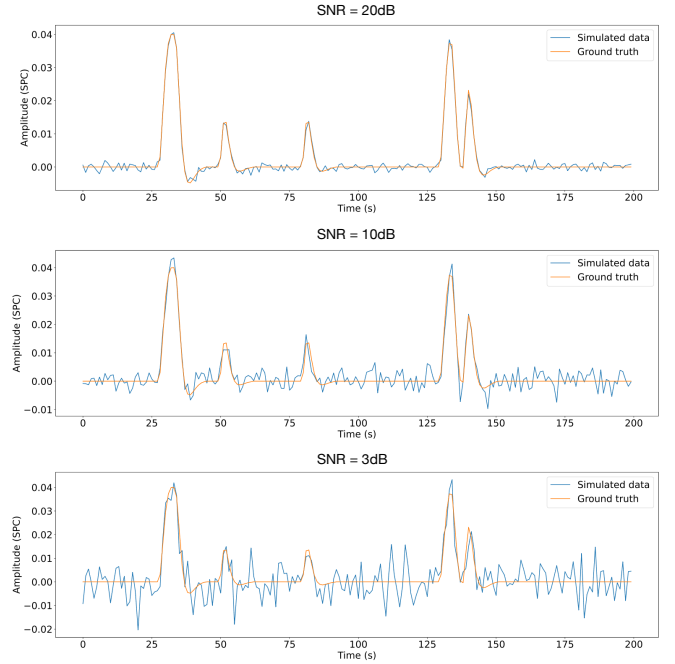


Figure 1: Simulated signal with different SNRs (20 dB, 10 dB and 3 dB).

52 slices, Partial-Fourier = 6/8, voxel size = 2.4x2.4x3 mm<sup>3</sup>, TR = 1.5 s, TEs = 10.6/28.69/46.78/64.87/82.96 ms, multiband factor = 4, flip angle = 70°, GRAPPA = 2). During the fMRI acquisition, subjects performed a motor task consisting of five different movements (left-hand finger tapping, right-hand finger tapping, moving the left toes, moving the right toes and moving the tongue). These conditions were randomly intermixed every 16 seconds, and were only repeated once the entire set of stimuli were presented. Data preprocessing consisted of optimally combining the echo time datasets, detrending of up to 5<sup>th</sup>-order Legendre polynomials, spatial smoothing (3 mm FWHM) and normalization to signal percentage change. For this comparison, we selected a voxel that best represented the right-hand finger-tapping paradigm as shown in Figure 2.

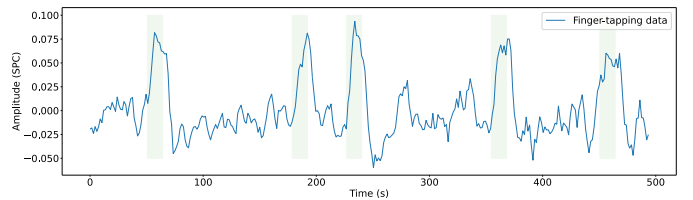


Figure 2: Most representative voxel of the finger-tapping task. Green blocks indicate the onsets and the duration of it.

**Resting-state datasets:** One healthy subject was scanned in a 3T MR scanner (Siemens) as part of a larger experiment under a Basque Center on Cognition, Brain and Language Review Board-approved protocol. Two runs

of T2\*-weighted fMRI data was acquired during resting state, each with 10 min duration, with 1) a standard gradient echo-planar imaging sequence (monoband) ( $TR = 2000$  ms,  $TE = 29$  ms, flip-angle =  $78^\circ$ , matrix size =  $64 \times 64$ , voxel size =  $3 \times 3 \times 3$  mm $^3$ , 33 axial slices with interleaved acquisition, slice gap = 0.6 mm) and 2) a simultaneous multislice gradient-echo echo-planar imaging sequence (multiband factor = 3) developed by the Center of Magnetic Resonance Research (University of Minnesota, USA) ( $TR = 800$  ms,  $TE = 29$  ms, flip-angle =  $60^\circ$ , matrix size =  $64 \times 64$ , voxel size =  $3 \times 3 \times 3$  mm $^3$ , 42 axial slices with interleaved acquisition, no slice gap). Single-band reference images were also collected in both resting-state acquisitions for head motion realignment. During both acquisitions, participants were instructed to keep their eyes open, fixating them in a white cross that they saw through a mirror located on the head coil, and not to think about anything specific. Field maps were also obtained to correct for field distortions.

### 3.2. Selection of the hemodynamic response function

With the aim of making a fair comparison of the two methods, we first compared their hemodynamic response functions. Figure 3A shows the difference in the hemodynamic response function that PFM and TA use by default for  $TR = 0.1$  s and  $TR = 1$  s adjusted to a peak amplitude of one; i.e. the SPMG1 and the HRF resulting from the linear differential operator. The most observable difference between the two HRF is the time to peak: the HRF used by Total Activation does not begin at zero while the one used by PFM does.

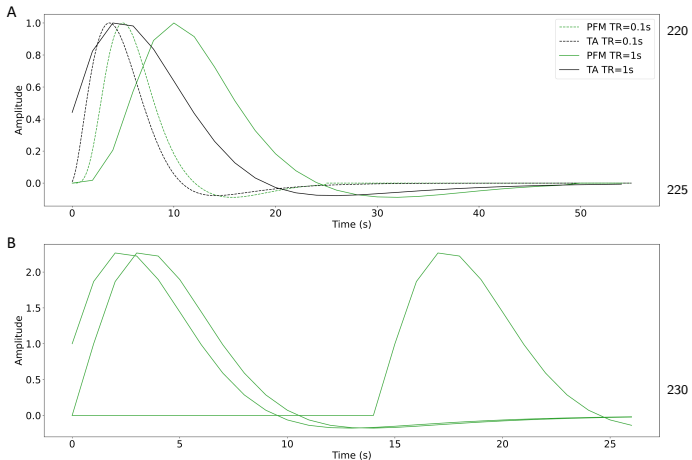


Figure 3: A) Canonical HRF models typically used by PFM (green) and TA (black) at  $TR = 0.1$  s (dashed lines) and  $TR = 1$  s (solid lines). Without loss of generality, the waveforms are scaled to unit amplitude for visualization. B) Representation of three shifted HRFs at  $TR=1$  s (onsets=0, 1, and 15 s) that build the design matrix for PFM when the HRF model has been matched to that in TA.

While Paradigm Free Mapping allows for the use of any hemodynamic response function — the columns of the design matrix  $\mathbf{H}$  are composed by shifted versions of the

HRF — the linear differential operator in TA is tailored for a fixed HRF. Hence, for practical reasons, we reproduced the HRF in the Total Activation filter and incorporated it into the PFM formulation (Figure 3B).

### 3.3. Selection of the regularization parameter based on the estimation of the noise

Total Activation proposes to solve the inverse problem by updating the regularization parameter  $\lambda$  on every iteration  $n$  so that the residuals converge to a previously estimated noise level of the data fit  $\tilde{\sigma}$ , where this pre-estimated noise is calculated from the median absolute deviation of fine-scale wavelet coefficients (Daubechies, order 3) [18]:

$$\lambda^{n+1} = \frac{N\tilde{\sigma}}{\frac{1}{2}\|\mathbf{y} - \mathbf{x}^n\|_F^2}\lambda^n. \quad (10)$$

Thus, we calculated the regularization path with PFM (as described in 3.4) and selected the  $\lambda$  corresponding to the residuals that were closest to the estimated noise level of the data. We applied Total Activation with temporal regularization in its original form. Figure 4 depicts the estimated activity-inducing, innovation and activity-related signals when updating  $\lambda$  as in (10) in the three simulated SNR settings using the spike model (left) and the block model (right). Figure 4 (left) shows nearly identical results between PFM (left) and TA (right). The minimal differences are the result of slight dissimilarities in the convergence of the residuals to the estimated noise level of the data. Likewise, the use of the block model with a selection of  $\lambda$  based on the convergence of the residuals to have the same variances as the MAD estimate of the noise yields results that are identical in practice as shown in Figure 4 (right).

In addition, we performed the same comparison on experimental data as introduced in 3.1. Figure 5 (row 3) illustrates that the estimated activity-inducing, innovation and activity-related signals with PFM and TA are once again practically identical both for the spike model (left) and the block model (right).

### 3.4. Selection of the regularization parameter by solving the regularization path

Paradigm Free Mapping bases its selection of the regularization parameter on the Bayesian Information Criterion (BIC) [19] and the Akaike Information Criterion (AIC) [20]. Hence, we calculated the regularization path with PFM by means of the least angle regression (LARS) algorithm [28] and used the  $\lambda$  in the path to solve the deconvolution problem with Total Activation.

Figure 6 (left) shows the regularization path of PFM and TA side by side for the three SNR conditions for the spike model; i.e., the inverse problem described in (3). Each iteration of LARS reduces the value of  $\lambda$ ; i.e., reduces the sparsity promoted by the  $l_1$ -norm, and reveals a new non-zero coefficient as shown in the x axis of the heatmaps. Vertical black lines depict the selection of the

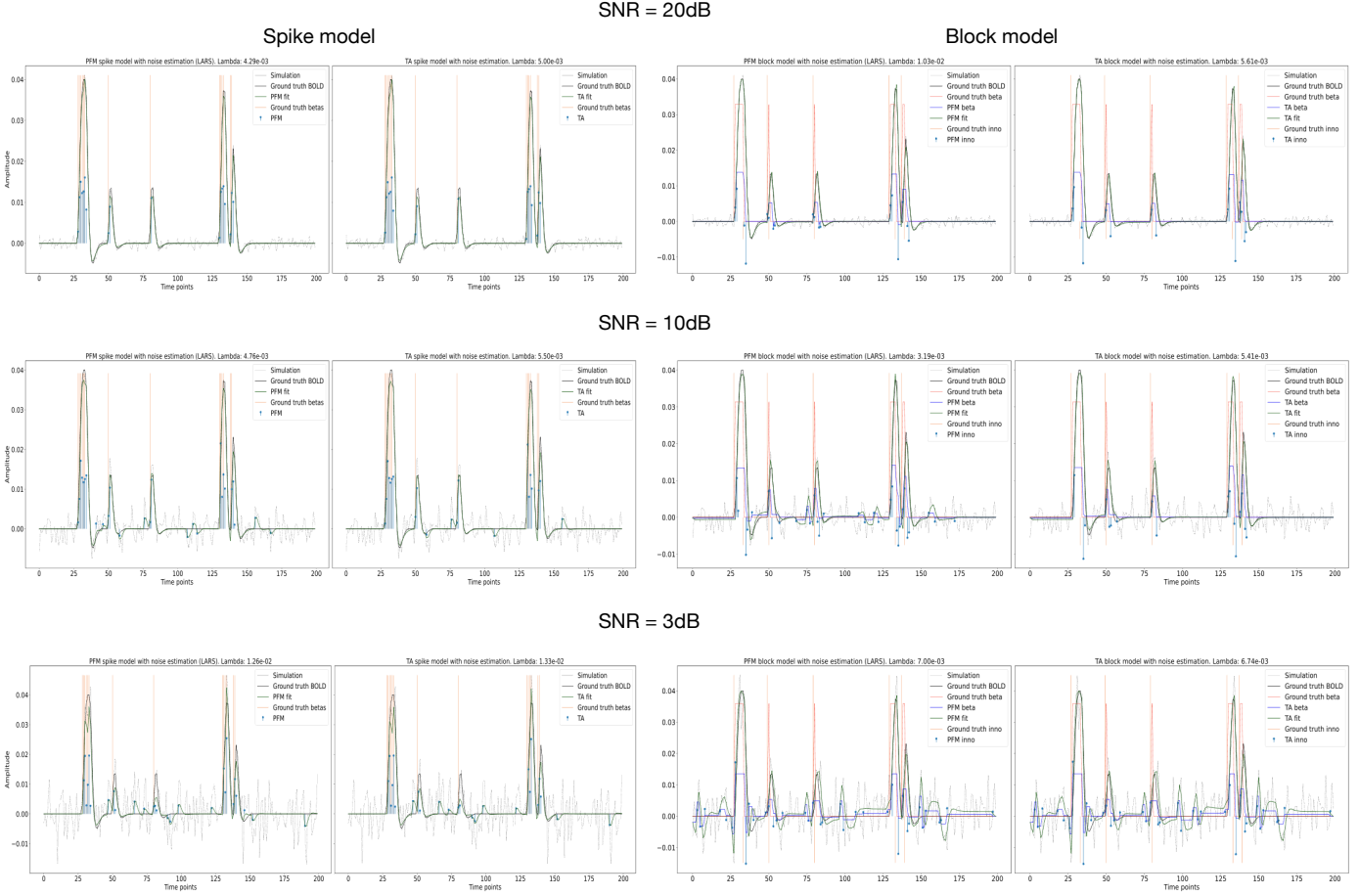


Figure 4: Estimated activity-inducing, innovation and activity-related (fit,  $\mathbf{x}$ ) signals when  $\lambda$  is selected based on convergence of residuals to have same variance as MAD estimate of noise with spike model (left, with PFM on the left and TA on the right) and block model (right, with PFM on the left and TA on the right) on SNR = 20dB (top), SNR = 10dB (middle) and SNR = 3dB (bottom).

regularization parameter based on BIC and AIC, and thus, the colored coefficients to the left of the vertical lines depict the estimated activity-inducing signal  $s(t)$ . Figure 6 (right) illustrates the resulting estimation of the activity-inducing and neuronal-related signals when basing the selection of  $\lambda$  on BIC for the three simulated SNR conditions. Given that the regularization paths of both techniques are identical, the BIC-based selection of the regularization parameter and the results of deconvolving with said  $\lambda$  are identical too (see Figure 9). Thus, Figure 6 demonstrates that, regardless of the simulated SNR condition, both deconvolution algorithms produce identical regularization paths when the same HRF and regularization parameters are applied, and hence, identical estimates of the activity-inducing signal  $\mathbf{s}$  and neuronal-related signal  $\mathbf{x}$ .

The regularization path to estimate innovation signals; i.e., solving the optimization problem using the block model in (4), yields mainly undistinguishable results for both PFM and TA methods as shown in Figure 7 (left). Again, the BIC-based selection of  $\lambda$  is identical for both PFM and TA and the estimation of the innovation signal  $\mathbf{u}$  shows

no distinguishable differences between the algorithms (see Figure 7 right). Figure 9 (right) demonstrates that the Therefore, both Paradigm Free Mapping and Total Activation yield nearly-identical regularization paths and estimates of the innovation signal regardless of the simulated SNR condition when applying the same HRF and regularization parameters with the block model.

Furthermore, we performed the same analysis on experimental data as shown in Figure 5 (rows 1-2, 4). Row 1 demonstrates that the PFM and TA regularization paths are identical when deconvolving experimental data, regardless of the deconvolution model (spike or block). Even though tiny differences can be seen between the two methods in the BIC and AIC selection of  $\lambda$  in row 4, row 2

## 4. Discussion

This work demonstrates that Paradigm Free Mapping and Total Activation yield practically identical results when the same HRF model and regularization parameter are employed, demonstrating that synthesis and analysis models

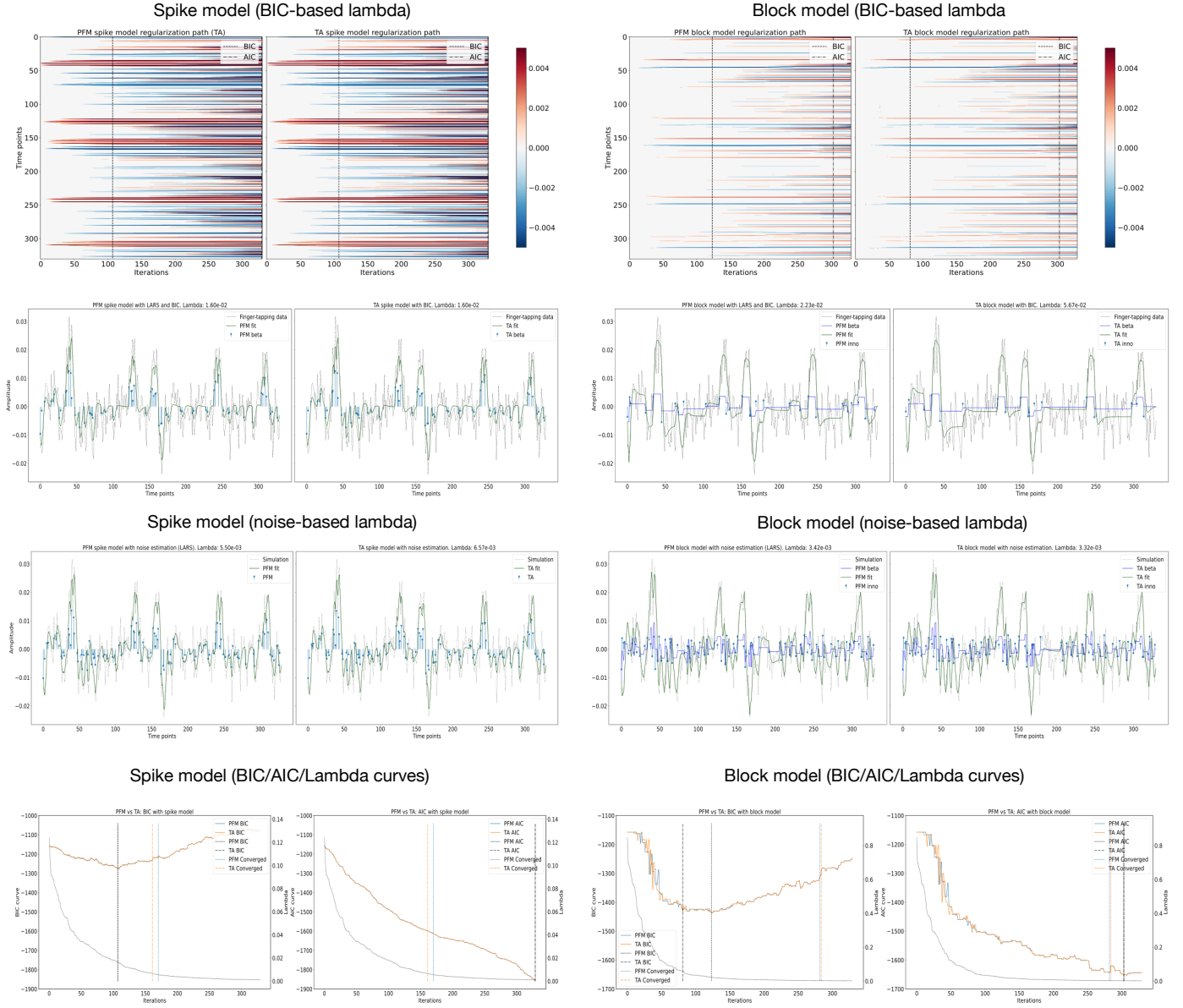


Figure 5: (Row 1) Regularization paths of the estimated activity-inducing signal (spike model — left) and innovation signal (block model — right); (Row 2) activity-inducing, innovation and activity-related (fit,  $\mathbf{x}$ ) signals when  $\lambda$  is selected based on BIC, or (Row 3) based on convergence of residuals to have same variance as MAD estimate of noise; (Row 4) Corresponding curves of BIC and AIC, where the vertical lines indicate the three options to select  $\lambda$  (BIC, AIC and Converged/MAD).

are equivalent for temporal fMRI deconvolution. Thus, previously observed differences in performance must be<sup>295</sup> due to differences in usage options. With the equivalence in the temporal deconvolution demonstrated, it is reasonable to assume that additional regularization terms in the spatial or temporal domains would not modify this equivalence when convex operators are employed; e.g. when the<sup>300</sup> regularization problem can be solved by means of the Fast Iterative Shrinkage-Thresholding Algorithm (FISTA) [29] or the Generalized Forward-Backward Splitting [30] techniques.

Taking into account the advantages and disadvantages of the presented techniques shown in Table 1, future work will improve and extend deconvolution methods for fMRI. For instance, the appropriate formulation depending on data acquisition (i.e. single-echo vs multi-echo) could be studied and compared with existing methods [31], or formulations that account for HRF variability could be investigated too [32, 33, 34]. Furthermore, robust methods to select the regularization parameter [35] and other potential  $\ell_{p,q}$ -norm regularization terms (e.g.  $p < 1$ ) or debiasing approaches could be explored.

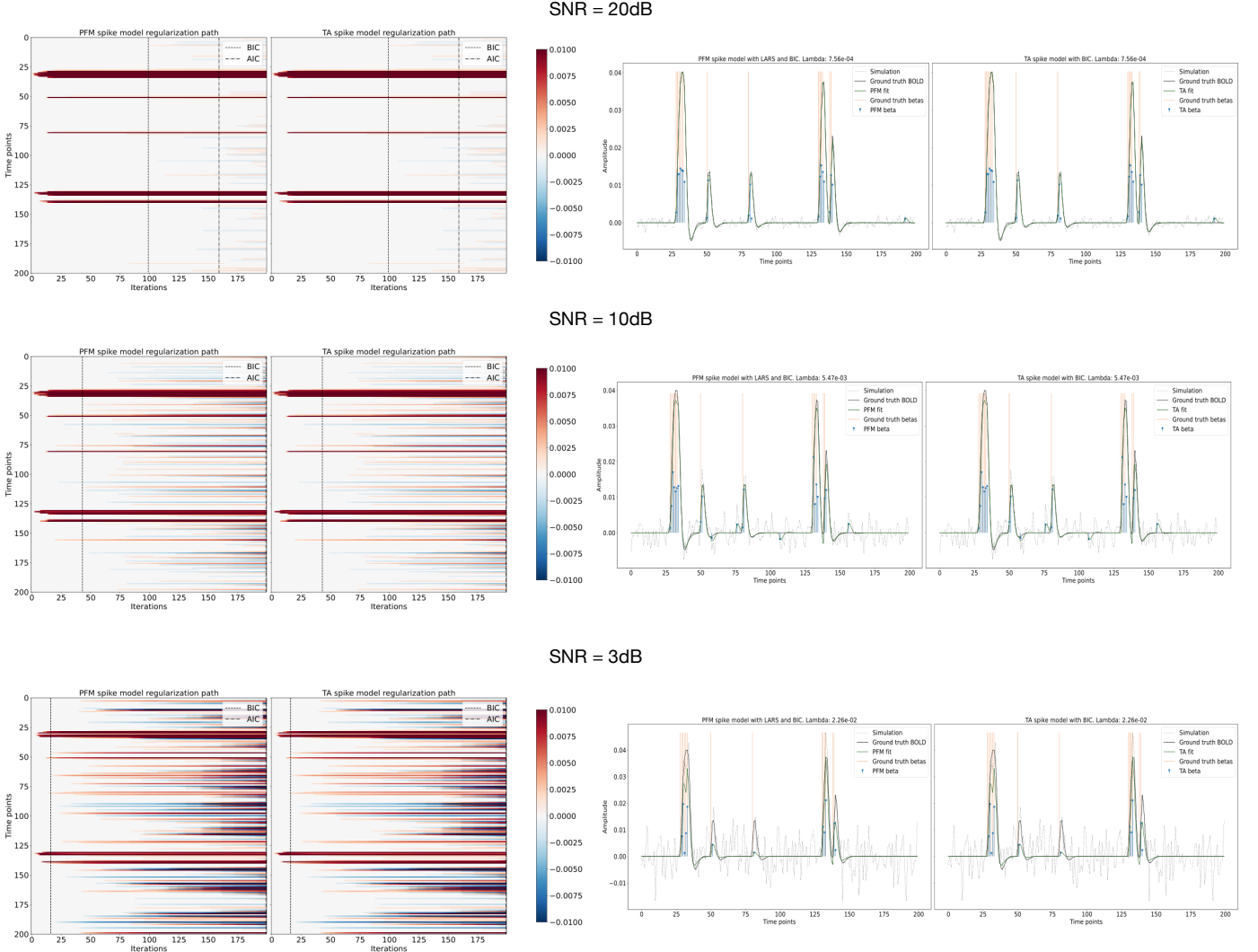


Figure 6: Spike model simulations. (Left) Heatmap of the regularization paths of the activity-inducing signal estimated with PFM and TA as a function of (increasing number of iterations in x-axis), whereas each row in the y-axis shows one time-point. Vertical lines denote iterations corresponding to the Akaike and Bayesian Information Criteria (AIC and BIC). (Right) Estimated activity-inducing (blue) and activity-related (green) signals when is set based on BIC. All estimates of are identical, regardless of SNR.

## Paradigm Free Mapping      Total Activation

305

## 5. Code availability

- + Can be extended to a multivariate problem.
- + Can be extended for multi-echo fMRI.
- + Can be used with any HRF.
- 

310

315

The code and materials used in this work can be found in the following GitHub repository: [https://github.com/eurunuela/pfm\\_vs\\_ta](https://github.com/eurunuela/pfm_vs_ta). We encourage the reader to play with the parameters (e.g. SNR, varying HRF options and mismatch between algorithms, TR, number of events, onsets, and durations) in the provided Jupyter notebooks.

## 6. Acknowledgements

This research was funded by the European Union’s Horizon 2020 research and innovation program (agreement No. 713673 of the Marie Skłodowska-Curie grant), La Caixa Foundation (ID 100010434, fellowship code LCF/B

Table 1: Advantages (+) and disadvantages (-) of Paradigm Free Mapping and Total Activation with respect to each other.

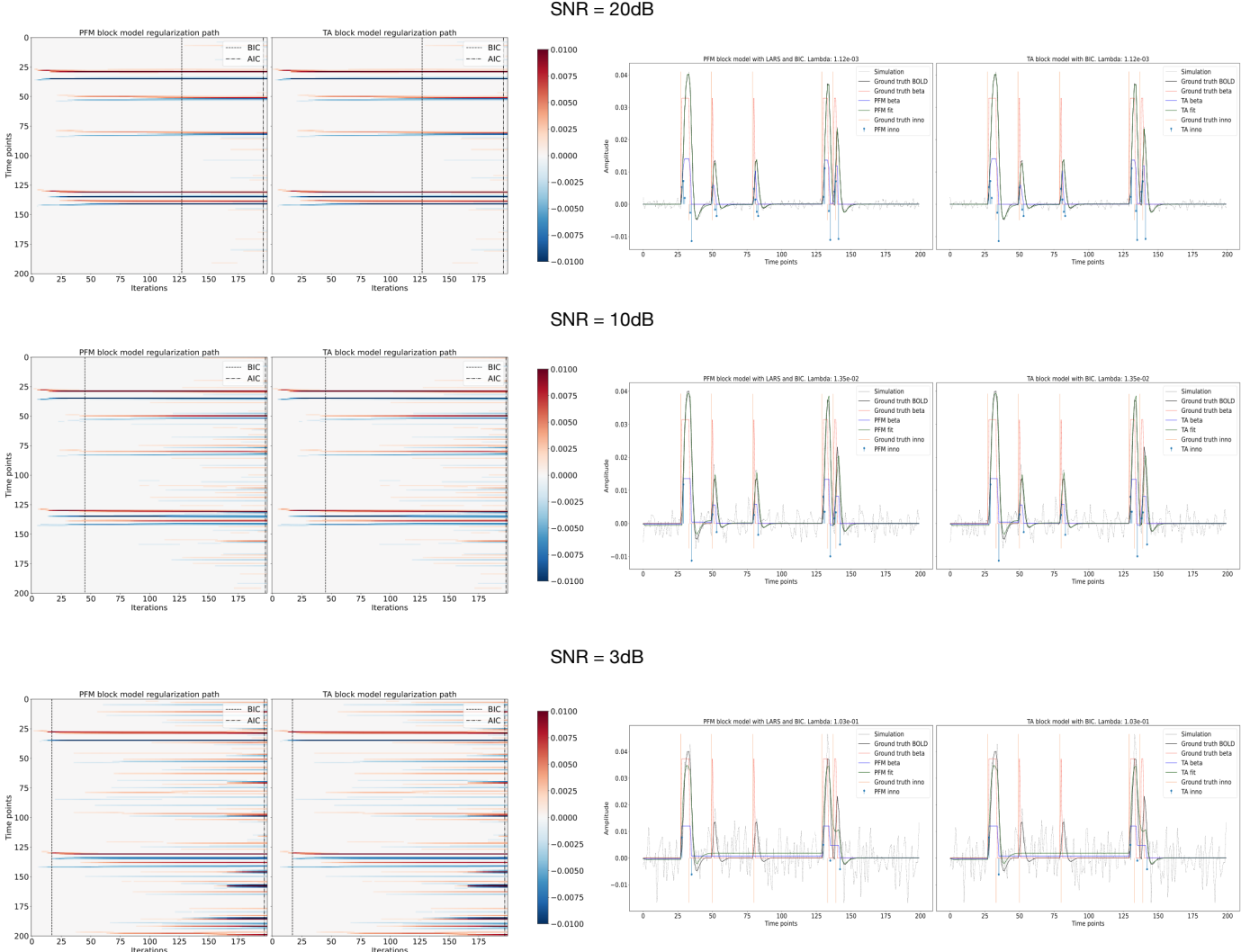


Figure 7: Block model simulations. (Left) Heatmap of the regularization paths of the innovation signal estimated with PFM and TA as a function of (increasing number of iterations in x-axis), whereas each row in the y-axis illustrates one time-point. Vertical lines denote iterations corresponding to the Akaike and Bayesian Information Criteria (AIC and BIC). (Right) Estimated innovation (blue) and activity-related (green) signals when is set based on BIC. All the estimates of are identical, regardless of SNR.

Q/IN17/11620063), the Spanish Ministry of Economy and Competitiveness (RYC-2017-21845), the Basque Government (BERC 2018-2021, PIBA\_2019\_104, PRE\_2019\_1\_005 320 4), and the Spanish Ministry of Science, Innovation and Universities (PID2019-105520GB-100).

## References

- [1] D. R. Gิตelman, W. D. Penny, J. Ashburner, K. J. Friston, Modeling regional and psychophysiologic interactions in fMRI: The importance of hemodynamic deconvolution, NeuroImage 19 (1) (2003) 200–207. doi:10.1016/S1053-8119(03)00058-2. 325 345
- [2] N. Petridou, C. C. Gaudes, I. L. Dryden, S. T. Francis, P. A. Gowland, Periods of rest in fMRI contain individual spontaneous events which are related to slowly fluctuating spontaneous activity, Human Brain Mapping 34 (6) (2013) 1319–1329. doi:10.1002/hbm.21513. 330 350
- [3] F. I. Karahanoglu, D. Van De Ville, Transient brain activity disentangles fMRI resting-state dynamics in terms of spatially and temporally overlapping networks, Nature Communications 6 (1) (2015) 7751. doi:10.1038/ncomms8751.
- [4] F. I. Karahanoglu, D. Van De Ville, Dynamics of large-scale fMRI networks: Deconstruct brain activity to build better models of brain function, Current Opinion in Biomedical Engineering 3 (2017) 28–36. doi:10.1016/j.cobme.2017.09.008.
- [5] N. Kinany, E. Pirondini, S. Micera, D. Van De Ville, Dynamic Functional Connectivity of Resting-State Spinal Cord fMRI Reveals Fine-Grained Intrinsic Architecture, Neuron 108 (3) (2020) 424–435.e4. doi:10.1016/j.neuron.2020.07.024.
- [6] J. Gonzalez-Castillo, C. Caballero-Gaudes, N. Topolski, D. A. Handwerker, F. Pereira, P. A. Bandettini, Imaging the spontaneous flow of thought: Distinct periods of cognition contribute to dynamic functional connectivity during rest, NeuroImage 202 (2019) 116129. doi:10.1016/j.neuroimage.2019.116129.
- [7] T. W. Allan, S. T. Francis, C. Caballero-Gaudes, P. G. Morris, E. B. Liddle, P. F. Liddle, M. J. Brookes, P. A. Gowland, Func-

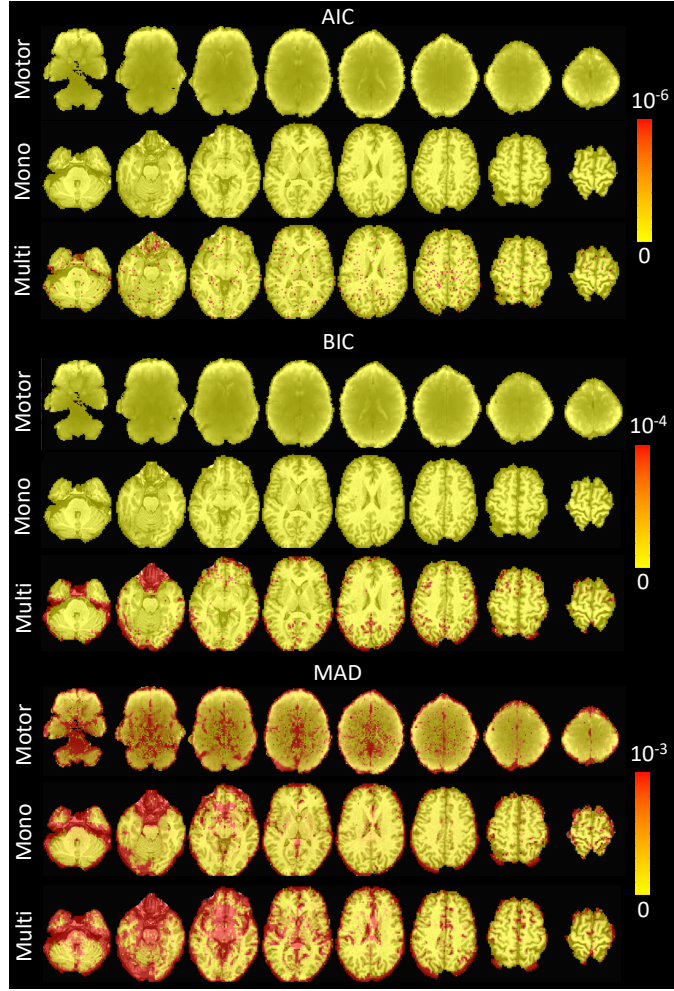


Figure 8: Sum of squares of the differences of the activity-inducing signals estimated with Paradigm Free Mapping and Total activation for the different selections of the regularization parameter: AIC (top), BIC (middle) and MAD (bottom). The sum of square difference maps are shown for the three experimental datasets introduced in section 3.1: the motor task (Motor), the monoband resting-state (Mono) and the multiband resting-state (Multi) datasets.

- tional connectivity in mri is driven by spontaneous bold events,<sup>375</sup> PLoS one 10 (4) (2015) e0124577.
- [8] F. Z. Esfahlani, Y. Jo, J. Faskowitz, L. Byrge, D. Kennedy, O. Sporns, R. Betzel, High-amplitude co-fluctuations in cortical activity drive functional connectivity, bioRxiv (2020) 800045.
- [9] E. S. Finn, P. A. Bandettini, Movie-watching outperforms<sup>380</sup> rest for functional connectivity-based prediction of behavior, bioRxiv (2020) 2020.08.23.263723–2020.08.23.263723doi:10.1101/2020.08.23.263723.
- [10] E. S. Finn, E. Glerean, A. Y. Khojandi, D. Nielson, P. J. Molfese, D. A. Handwerker, P. A. Bandettini, Idiosynchrony:<sup>385</sup> From shared responses to individual differences during naturalistic neuroimaging, NeuroImage 215 (April) (2020) 116828–116828. doi:10.1016/j.neuroimage.2020.116828.
- [11] R. F. Betzel, L. Byrge, F. Z. Esfahlani, D. P. Kennedy, Temporal fluctuations in the brain’s modular architecture during<sup>390</sup> movie-watching, NeuroImage 213 (2020) 116687. doi:10.1016/j.neuroimage.2020.116687.
- [12] J. Faskowitz, F. Z. Esfahlani, Y. Jo, O. Sporns, R. F. Betzel, Edge-centric functional network representations of human cerebral cortex reveal overlapping system-level architecture, Tech.<sup>395</sup> rep., Nature Publishing Group (2020).
- [13] G. Bommarito, A. Tarun, Y. Farouj, M. G. Preti, M. Petracca, A. Drobny, M. M. El Mendili, M. Inglesie, D. Van De Ville, Functional network dynamics in progressive multiple sclerosis, medRxiv.
- [14] D. Zöller, C. Sandini, F. I. Karahanoglu, M. C. Padula, M. Schaer, S. Eliez, D. Van De Ville, Large-scale brain network dynamics provide a measure of psychosis and anxiety in 22q11.2 deletion syndrome, Biological Psychiatry: Cognitive Neuroscience and Neuroimaging 4 (10) (2019) 881–892.
- [15] R. Lopes, J.-M. Lina, F. Fahoum, J. Gotman, Detection of epileptic activity in fmri without recording the eeg, Neuroimage 60 (3) (2012) 1867–1879.
- [16] A. Tarun, D. Wainstein-Andriano, V. Sterpenich, L. Bayer, L. Perogamvros, M. Solms, N. Axmacher, S. Schwartz, D. Van De Ville, Nrem sleep stages specifically alter dynamical integration of large-scale brain networks, Iscience 24 (1) (2020) 101923.
- [17] C. Caballero Gaudes, N. Petridou, S. T. Francis, I. L. Dryden, P. A. Gowland, Paradigm free mapping with sparse regression automatically detects single-trial functional magnetic resonance imaging blood oxygenation level dependent responses, Human Brain Mappingdoi:10.1002/hbm.21452.
- [18] F. I. Karahanoglu, C. Caballero-Gaudes, F. Lazeyras, D. Van De Ville, Total activation: FMRI deconvolution through spatio-temporal regularization, NeuroImagedoi:10.1016/j.neuroimage.2013.01.067.
- [19] G. Schwarz, Estimating the Dimension of a Model, Annals of

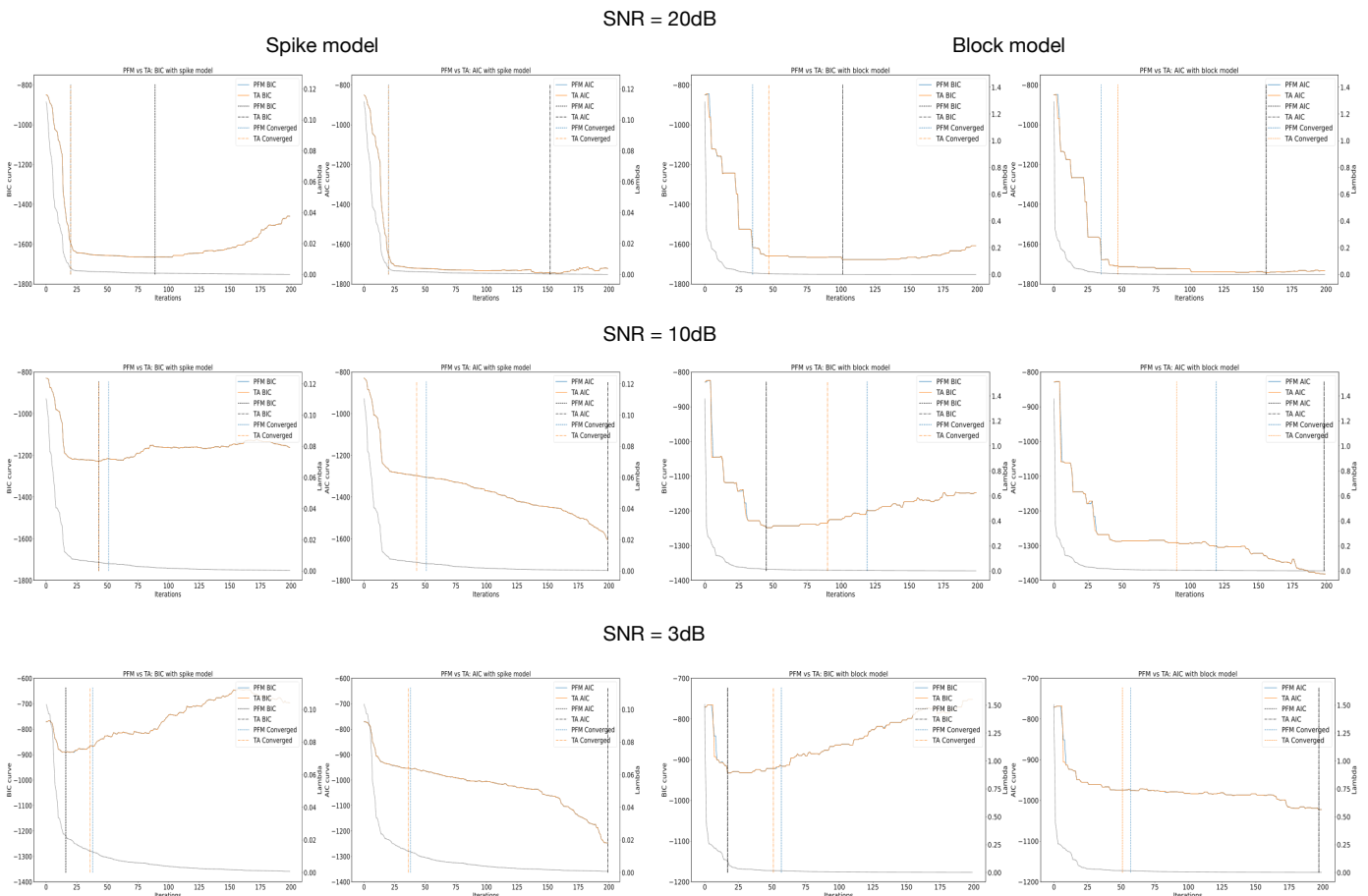


Figure 9: Lambdas and cost.

- Statistics 6 (2) (1978) 461–464. doi:10.1214/aos/1176344136.
- [20] H. Akaike, Information Theory and an Extension of the Maximum Likelihood Principle, in: E. Parzen, K. Tanabe, G. Kitagawa (Eds.), Selected Papers of Hirotugu Akaike, Springer Series in Statistics, Springer, New York, NY, 1998, pp. 199–213. doi:10.1007/978-1-4612-1694-0\_15.
- [21] H. Cherkaoui, T. Moreau, A. Halimi, P. Ciuciu, Sparsity-based Blind Deconvolution of Neural Activation Signal in fMRI, in: ICASSP 2019 - 2019 IEEE International Conference on Acoustics, Speech and Signal Processing (ICASSP), 2019, pp. 1323–1327. doi:10.1109/ICASSP.2019.8683358.
- [22] E. Uruñuela, S. Jones, A. Crawford, W. Shin, S. Oh, M. Lowe, C. Caballero-Gaudes, Stability-Based Sparse Paradigm Free Mapping Algorithm for Deconvolution of Functional MRI Data, Proceedings of the Annual International Conference of the IEEE Engineering in Medicine and Biology Society, EMBS 2020-July (2020) 1092–1095. doi:10.1109/EMBC44109.2020.9176137.
- [23] C. C. Gaudes, N. Petridou, I. L. Dryden, L. Bai, S. T. Francis, P. A. Gowland, Detection and characterization of single-trial fMRI bold responses: Paradigm free mapping, Human Brain Mapping doi:10.1002/hbm.21116.
- [24] A. M. Bruckstein, D. L. Donoho, M. Elad, From Sparse Solutions of Systems of Equations to Sparse Modeling of Signals and Images, SIAM Review 51 (1) (2009) 34–81. doi:10.1137/060657704.
- [25] R. Tibshirani, Regression Shrinkage and Selection Via the Lasso, Journal of the Royal Statistical Society: Series B (Methodological) 58 (1) (1996) 267–288. doi:10.1111/j.2517-6161.1996.tb02080.x.
- [26] I. Khalidov, J. Fadili, F. Lazeyras, D. Van De Ville, M. Unser, Activelets: Wavelets for sparse representation of hemodynamic responses, Signal processing 91 (12) (2011) 2810–2821.
- [27] F. I. Karahanoglu, İ. Bayram, D. V. D. Ville, A Signal Processing Approach to Generalized 1-D Total Variation, IEEE Transactions on Signal Processing 59 (11) (2011) 5265–5274. doi:10.1109/TSP.2011.2164399.
- [28] B. Efron, T. Hastie, I. Johnstone, R. Tibshirani, Least Angle Regression, The Annals of Statistics 32 (2) (2004) 407–499. doi:10.1214/009053604000000067.
- [29] A. Beck, M. Teboulle, A fast iterative shrinkage-thresholding algorithm, Society for Industrial and Applied Mathematics Journal on Imaging Sciences 2 (1) (2009) 183–202. doi:10.1137/080716542.
- [30] H. Raguet, J. Fadili, G. Peyré, A Generalized Forward-Backward Splitting, SIAM Journal on Imaging Sciences 6 (3) (2013) 1199–1226. doi:10.1137/120872802.
- [31] C. Caballero-Gaudes, S. Moia, P. Panwar, P. A. Bandettini, J. Gonzalez-Castillo, A deconvolution algorithm for multi-echo functional mri: Multi-echo sparse paradigm free mapping, NeuroImage 202 (2019) 116081.
- [32] S. Badillo, T. Vincent, P. Ciuciu, Group-level impacts of within- and between-subject hemodynamic variability in fmri, Neuroimage 82 (2013) 433–448.
- [33] C. C. Gaudes, F. I. Karahanoglu, F. Lazeyras, D. Van De Ville, Structured sparse deconvolution for paradigm free mapping of functional mri data, in: 2012 9th IEEE International Symposium on Biomedical Imaging (ISBI), IEEE, 2012, pp. 103–106. doi:10.1109/ISBI.2012.6231910.

- 455 sium on Biomedical Imaging (ISBI), IEEE, 2012, pp. 322–325.
- [34] Y. Farouj, F. I. Karahanoglu, D. Van De Ville, Bold signal deconvolution under uncertain haemodynamics: A semi-blind approach, in: 2019 IEEE 16th International Symposium on Biomedical Imaging (ISBI 2019), IEEE, 2019, pp. 1792–1796.
- 460 [35] N. Meinshausen, P. Bühlmann, Stability selection, *Journal of the Royal Statistical Society: Series B (Statistical Methodology)* 72 (4) (2010) 417–473.